

# Nonlinear Oscillations and Bifurcations in Silicon Microdisk Resonators: Supplemental Material

Daniel M. Abrams,<sup>1,2,3,\*</sup> Alex Slawik,<sup>1,†</sup> and Kartik Srinivasan<sup>4,‡</sup>

<sup>1</sup>*Department of Engineering Sciences and Applied Mathematics, Northwestern University, Evanston, IL 60208*

<sup>2</sup>*Northwestern Institute on Complex Systems, Northwestern University, Evanston, IL 60208*

<sup>3</sup>*Department of Physics & Astronomy, Northwestern University, Evanston, IL 60208*

<sup>4</sup>*Center for Nanoscale Science and Technology, National Institute of Standards and Technology, Gaithersburg, MD 20899*

(Dated: January 16, 2014)

## S1. EXPERIMENTAL DETAILS

Silicon microdisk cavities are fabricated in a silicon-on-insulator wafer with a 260 nm thick Si layer, 1  $\mu\text{m}$  thick buried silicon dioxide layer, and specified device layer resistivity of 13.5 ohm-cm to 22.5 ohm-cm (p-type). Fabrication steps included electron-beam lithography of a 350 nm-thick positive-tone resist, an  $\text{SF}_6/\text{C}_4\text{F}_8$  inductively-coupled plasma reactive ion etch through the silicon layer, a stabilized  $\text{H}_2\text{SO}_4/\text{H}_2\text{O}_2$  etch to remove the remnant resist and other organic materials, and an HF wet etch to undercut the disks.

Devices were characterized (Fig. S1(a)) using a swept-wavelength external cavity tunable diode laser with a time-averaged linewidth less than 90 MHz and absolute stepped wavelength accuracy of 1 pm. Light is coupled into and out of the cavities using an optical fiber taper waveguide in a  $\text{N}_2$ -purged environment at atmospheric pressure and room temperature. Cavity transmission spectra were recorded using a InGaAs photoreceiver, while radio frequency (RF) spectra were recorded using a 0 MHz (DC) to 125 MHz InGaAs photoreceiver whose output was sent into an electronic spectrum analyzer.

Figure S1(b) shows a typical RF spectrum for a microdisk pumped with  $P_{\text{in}} \approx 400 \mu\text{W}$  at a fixed laser-cavity detuning, while Fig. S1(c),(d) compiles a series of such spectra as a function of laser-cavity detuning. Spectra such as these are analyzed to produce the period and amplitude data in Figs. 5 and 6 in the main text. Spectra are not shown for detunings where no oscillations occur (i.e., where the time domain signal is constant).

The discontinuity in Fig. S1(c) is a result of a transition between two resonant modes in the microdisk cavity. Data presented in Fig. 5 of the main text is restricted to a single mode consistent with our model.

## S2. PHYSICAL ORIGIN OF EQUATIONS

The section titled “Physical system and model” in the main text gives a concise explanation of the physical origin of Eqs. (1a)–(1c). Here, we expand on this by presenting a schematic of the model in Figure S2 and an explanation of all the model variables and parameters in Table S1. For a more extensive derivation, however, we refer the interested reader to the 2006 publication by Johnson, Borselli and Painter [1].

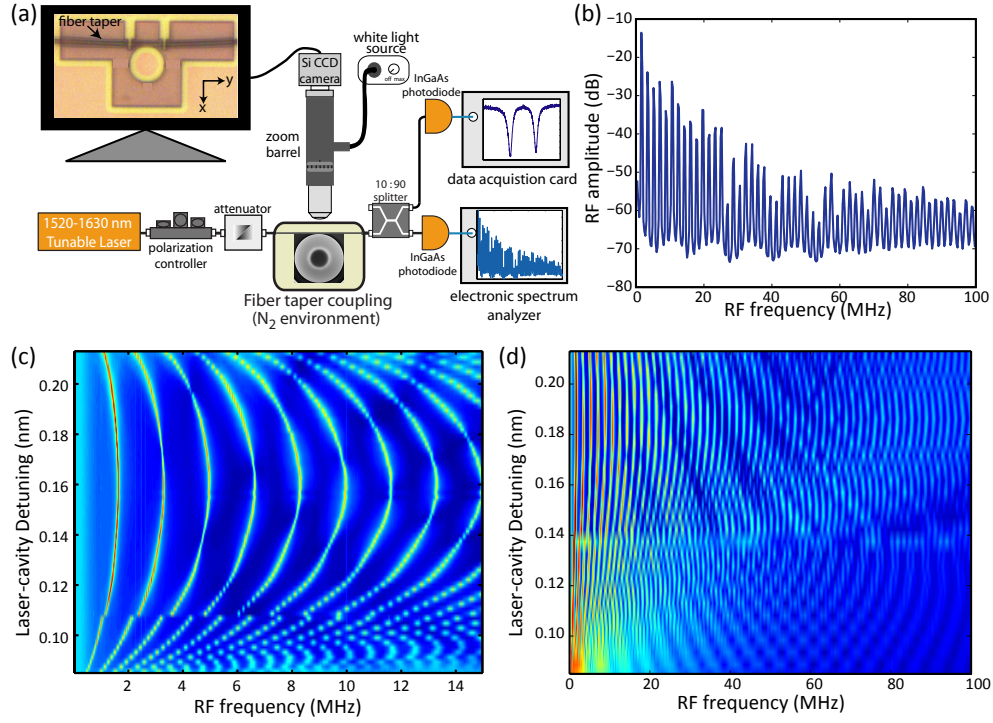


FIG. S1. (a) Experimental setup for measuring the silicon microdisk cavities. (b) RF spectrum of a microdisk for  $P_{in} \approx 400 \mu\text{W}$  and fixed laser-cavity detuning. (c)-(d) RF spectra as a function of laser-cavity detuning (laser frequency is detuned below cavity resonance frequency).

Parameter	Meaning	Parameter	Meaning
$c$	Speed of light	$V_{eff}$	Volume of disk effectively occupied by resonant mode
$\hbar$	Planck's constant / $2\pi$	$V_{TPA}$	Disk volume effectively available for two-photon absorption
$\lambda_0$	Resonant wavelength of cavity mode	$V_{FCA}$	Disk volume effectively available for free carrier absorption
$n_{Si}$	Index of refraction for Si	$V_{disk}$	Physical volume of microdisk
$n_g$	Group index for the optical cavity mode	$Q$	Intrinsic quality factor for disk at low optical powers ( $Q = \omega_0/\gamma_0$ )
$c_p$	Heat capacity of Si	$\omega_0$	Resonant angular frequency of mode ( $\lambda_0 = 2\pi c/\omega_0$ )
$\sigma_{Si}$	Free carrier absorption cross section	$\gamma_0$	Decay rate of EM field due to radiation and linear absorption
$\beta_{Si}$	Two-photon absorption parameter	$\gamma_e$	Decay rate of EM field due to coupling to the access waveguide ("extrinsic")
$\rho_{Si}$	Density of Si	$\gamma_{lin}$	Decay rate of the EM field due to linear optical absorption
$\frac{dn_{Si}}{dN}$	Free-carrier effect on index of refraction	$\gamma_{fc}$	Free carrier decay rate (inverse of free-carrier lifetime)
$\frac{dn_{Si}}{dT}$	Temperature effect on index of refraction	$\gamma_{Th}$	Thermal decay rate (inverse of thermal lifetime)
$\Gamma_{disk}$	Fractional energy overlap with $\Delta T$ within the microdisk	$P_{in}$	Power input (optical)
$\Gamma_{TPA}$	Overlap factor for two-photon absorption	$\delta\omega_0$	Detuning of input signal from resonance
$\Gamma_{FCA}$	Overlap factor for free-carrier absorption	$\kappa$	Coupling loss between fiber and disk

TABLE S1. Definitions of variables and parameters from model.

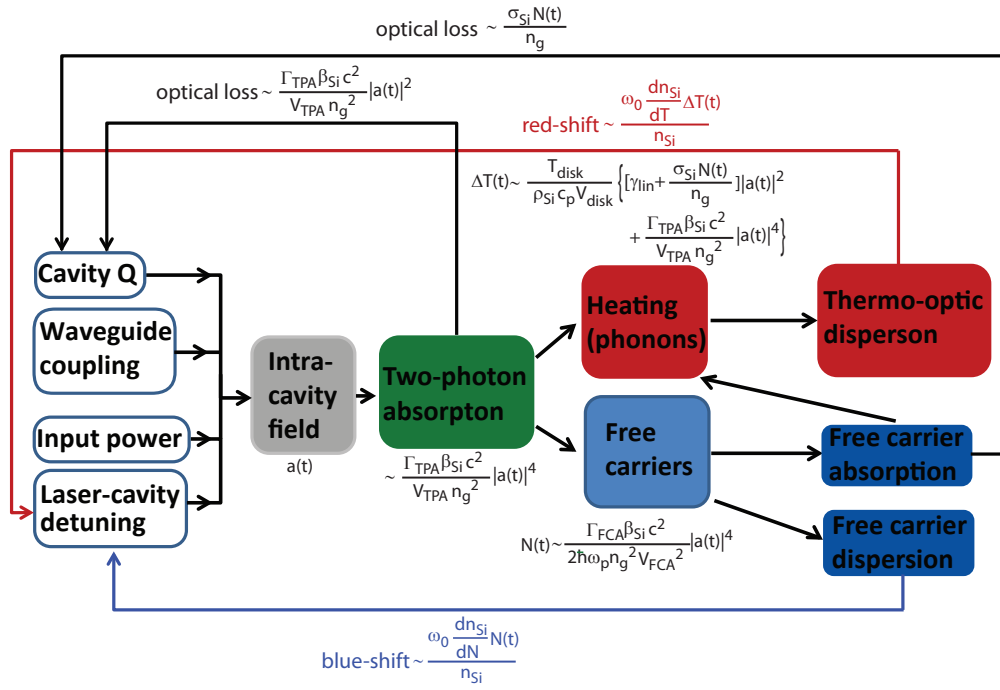


FIG. S2. Illustration of the different physical processes considered in the model, as represented by the equations of motion (Eqs. (1a)-(1c) in the main text). The intracavity optical field  $a(t)$  is determined by the input optical power, waveguide coupling rate, laser-cavity detuning, and cavity  $Q$  factor. A strong intracavity field leads to two-photon absorption, which reduces the cavity  $Q$  while also generating heat and free carriers. The added heat produces thermo-optic dispersion and results in a red-shift of the cavity mode with respect to the laser, while the generated free carriers lead to absorption and dispersion. Free-carrier absorption reduces the cavity  $Q$  while also potentially leading to additional heating and thermo-optic dispersion, while free-carrier dispersion results in a blue shift of the cavity with respect to the laser.

### S3. DIMENSIONAL CONSTANTS:

Table S2 lists the dimensional constants used in the model. Values given are those used in calculation unless otherwise specified.

Parameter	Value	Source	Parameter	Value	Source
$c$	$2.998 \times 10^8$ m/s	physical const.	$V_{eff}$	$50 \left( \frac{\lambda_0}{n_{Si}} \right)^3 = 3.99 \times 10^{-18}$ m <sup>3</sup>	FEM [1] *
$\hbar$	$1.05 \times 10^{-34}$ J s	physical const.	$V_{TPA}$	$2V_{eff} = 7.97 \times 10^{-18}$ m <sup>3</sup>	FEM [1] *
$\lambda_0$	$1.5 \times 10^{-6}$ m	low-power meas. *	$V_{FCA}$	$2V_{eff} = 7.97 \times 10^{-18}$ m <sup>3</sup>	FEM [1] *
$n_{Si}$	3.485	material const.	$V_{disk}$	$10V_{eff} = 3.99 \times 10^{-17}$ m <sup>3</sup>	FEM [1] *
$n_g$	3.485	material const.	$Q$	$3 \times 10^5$	low-power meas. *
$c_p$	700 J/(kg K)	material const.	$\omega_0$	$\frac{2\pi c}{\lambda_0} = 1.26 \times 10^{15}$ Hz	low-power meas. *
$\sigma_{Si}$	$10^{-21}$ m <sup>2</sup>	material const.	$\gamma_0$	$\frac{2\pi c}{\lambda_0 Q} = 4.19 \times 10^9$ Hz	low-power meas. *
$\beta_{Si}$	$8.4 \times 10^{-12}$ m/W	material const.	$\gamma_e$	$\frac{2\pi c}{\lambda_0 Q} = 4.19 \times 10^9$ Hz	critical coupling *
$\rho_{Si}$	2330 kg/m <sup>3</sup>	material const.	$\gamma_{lin}$	$\frac{2\pi c}{\lambda_0 Q} = 4.19 \times 10^9$ Hz	no radiation loss *
$\frac{dn_{Si}}{dN}$	$-1.73 \times 10^{-27}$ m <sup>3</sup>	material const.	$\gamma_{fc}$	$10^8$ Hz	[1]
$\frac{dn_{Si}}{dT}$	$1.86 \times 10^{-4}$ K <sup>-1</sup>	material const.	$\gamma_{Th}$	$2 \times 10^5$ Hz	[1] *
$\Gamma_{disk}$	1	FEM [1]	$P_{in}$	in range 30 $\mu$ W – 3160 $\mu$ W	measured
$\Gamma_{TPA}$	1	FEM [1]	$\delta\omega_0$	in range 0 Hz – $3.3 \times 10^{11}$ Hz	measured
$\Gamma_{FCA}$	1	FEM [1]	$\kappa$	$\sqrt{\gamma_e} = 6.47 \times 10^5 \sqrt{\text{Hz}}$	critical coupling *

TABLE S2. Constants used for simulation and analysis. Values of parameters (\*) used for comparison to laboratory data in Fig. 5 of the main text are given in figure caption.

#### S4. NONDIMENSIONAL CONSTANTS:

Consider the nondimensional equations

$$\frac{dU}{d\tau} = -A_1U - A_2S^2U(U^2 + V^2) - A_3\eta U + A_4\eta V + A_5xV - A_6\theta V, \quad (\text{S1a})$$

$$\frac{dV}{d\tau} = -A_1V - A_2S^2V(U^2 + V^2) - A_3\eta V - A_4\eta U - A_5xU + A_6\theta U - A_7, \quad (\text{S1b})$$

$$\frac{d\eta}{d\tau} = -A_8\eta + A_9S^4(U^2 + V^2)^2, \quad (\text{S1c})$$

$$\frac{d\theta}{d\tau} = -A_{10}\theta + A_{11}S^2(U^2 + V^2) + A_{12}S^4(U^2 + V^2)^2 + A_{13}S^2\eta(U^2 + V^2), \quad (\text{S1d})$$

resulting from a nondimensionalization of the form

$$\begin{aligned} \tau &= c_1 t, \\ U(\tau) &= \frac{1}{c_2} \text{Re}(a(t)), \\ V(\tau) &= \frac{1}{c_2} \text{Im}(a(t)), \\ \eta(\tau) &= \frac{1}{c_3} N(t), \\ \theta(\tau) &= \frac{1}{c_4} \Delta T(t), \end{aligned}$$

with

$$\begin{aligned} c_1 &= \frac{\gamma_0}{\sqrt{Q}}, \\ c_2 &= \frac{6Q^{1/4}\sqrt{P_{in}}}{\sqrt{\omega_0}}, \\ c_3 &= \frac{Q}{V_{eff}}, \\ c_4 &= \frac{\gamma_0^2 \sigma_{Si} Q}{c_p}. \end{aligned}$$

The system is non-dimensionalized with a characteristic time, length, mass, and temperature scale. Here we have taken

$$\begin{aligned} [\text{time}] &= \gamma_0^{-1} \\ [\text{length}] &= V_{eff}^{1/3} \\ [\text{mass}] &= \frac{P_{in}}{\gamma_0^3 V_{eff}^{2/3}} \\ [\text{temp.}] &= \frac{\gamma_0^2 \sigma_{Si}}{c_p}, \end{aligned}$$

The quality factor  $Q$  was used to scale the dynamic variables to ranges of  $\mathcal{O}(1)$ .  $A_1$  through  $A_{13}$  are positive real constants, given as follows:

Control Parameter	Expression	Range
$x$	$\frac{\delta\omega_0}{\gamma_0}$	0-500, typical value 100
$S$	$\frac{sQ\sqrt{\beta_{Si}\omega_0}}{\sqrt{c}}$	0-100, typical value 56
Nondimensional Coefficient	Expression	Value
$A_1$	$\frac{\gamma_0 + \gamma_e \sqrt{Q}}{2 \gamma_0}$	547.72
$A_2 S^2$	$\left( \frac{18 \Gamma_{TPA} c^3}{V_{TPA} n_g^2 \gamma_0 \omega_0^2 Q} \right) S^2$	0.0025289 $S^2$ , typical value 7.9307
$A_3$	$\frac{\sigma_{Si} c Q^{3/2}}{2 \gamma_0 n_g V_{eff}}$	423.49
$A_4$	$-\frac{\omega_0 \frac{dn_{Si}}{dN} Q^{3/2}}{n_{Si} \gamma_0 V_{eff}}$	6137.8
$A_5 x$	$\left( \frac{\gamma_e \sqrt{Q}}{\gamma_0} \right) x$	547.72 $x$ , typical value $5.4772 \times 10^4$
$A_6$	$\frac{\omega_0 \frac{dn_{Si}}{dT} \gamma_0 \sigma_{Si} Q^{3/2}}{n_{Si} c_p}$	$6.5858 \times 10^4$
$A_7$	$\frac{\kappa Q^{1/4} \sqrt{\omega_0}}{6 \gamma_0}$	2136.4
$A_8$	$\frac{\gamma_{fc} \sqrt{Q}}{\gamma_0}$	13.085
$A_9 S^4$	$\left( \frac{648 \Gamma_{FCA} V_{eff} c^4}{\beta_{Si} \omega_0^4 Q^{7/2} h \omega_0 \gamma_0 n_g^2 V_{FCA}^2} \right) S^4$	$1.5849 \times 10^{-7} S^4$ , typical value 1.5589
$A_{10}$	$\frac{\gamma_{Th} \sqrt{Q}}{\gamma_0}$	0.026152
$A_{11} S^2$	$\left( \frac{36 T_{disk} \gamma_{lin} c}{\rho_{Si} V_{disk} \beta_{Si} \omega_0^2 Q^2 \gamma_0^3 \sigma_{Si}} \right) S^2$	$5.5614 \times 10^{-6} S^2$ , typical value 0.017440
$A_{12} S^4$	$\left( \frac{1296 T_{disk} \Gamma_{TPA} c^4}{\beta_{Si} \rho_{Si} V_{disk} V_{TPA} n_g^2 \omega_0^4 Q^{7/2} \gamma_0^3 \sigma_{Si}} \right) S^4$	$5.1356 \times 10^{-11} S^4$ , typical value $5.0506 \times 10^{-4}$
$A_{13} S^2$	$\left( \frac{36 T_{disk} c^2}{\rho_{Si} V_{disk} n_g \beta_{Si} \omega_0^2 Q V_{eff} \gamma_0^3} \right) S^2$	$8.6000 \times 10^{-6} S^2$ , typical value 0.026970

TABLE S3. Non-dimensional parameters and their typical numerical values.  $x$  and  $S$  are control parameters while  $A_{1-13}$  are fixed parameters.

## S5. BIRTH OF LIMIT CYCLE

Consider a limit cycle of the state  $\vec{\psi}(\tau) = (U, V, \eta, \theta)$  parameterized by  $(x, S)$ . Call the region of parameter space where this limit cycle exists  $\Sigma$ . Define the limit cycle  $\vec{\psi}(t) = \vec{\psi}(t + T)$  as  $L_{x,S}$ , with period  $T$ .

The limit cycle is ‘‘born’’ in parameter space on the boundary  $\partial\Sigma$ , defined by a Hopf-condition with zero amplitude and non-zero period  $T$ . The Hopf-condition is the requirement that a pair of complex conjugate eigenvalues cross the imaginary axis. The limit cycle is either born stable (supercritical) or unstable (subcritical). We have identified numerically the point at which stability changes, which is visible in Fig. 3 (asterisk near  $P_{in} = 125 \mu\text{W}$ ,  $\delta\omega_0/\gamma_0 = 60$ ).

The limit cycle is born as a sinusoidal wave for each variable in time. To lowest order state variable  $\vec{\psi}_i \propto \sin(\frac{2\pi t}{T} + \alpha_i)$ , where  $\alpha_i$  is a phase lag parameter to be determined. In system (S1), define the difference in the parameters  $x$  and  $S$  from the Hopf bifurcation to be

$$\begin{aligned} x - x_{Hopf} &= \nu_1 \epsilon^2 \\ S - S_{Hopf} &= \nu_2 \epsilon^2, \end{aligned}$$

where  $\epsilon \ll 1$  and  $\nu_1$  and  $\nu_2$  are  $\mathcal{O}(1)$ . Assume the limit cycle can be expressed as a power series in  $\epsilon$ . As  $\epsilon \rightarrow 0$ , we expect the expansion to approach the true limit cycle asymptotically. The following series assumes that each variable can be expanded as a sum of a homogeneous part and a sinusoidal part, and was found to conveniently solve the system of equations in the limit of small  $\epsilon$ :

$$\begin{aligned}
U(\tau|\epsilon) &= U_H + U_{osc} = \sum_{n=0}^{\infty} \epsilon^{2n} U_n + \sum_{n=1}^{\infty} a_n \epsilon^n \cos^n(\omega\tau + \alpha_n) \\
\text{where } \omega &= \omega(\epsilon) = \sum_{k=0}^{\infty} \omega_k \epsilon^{2k}, \quad \alpha_n = \alpha_n(\epsilon) = \sum_{k=0}^{\infty} \alpha_{n,k} \epsilon^{2k} \\
V(\tau|\epsilon) &= V_H + V_{osc} = \sum_{n=0}^{\infty} \epsilon^{2n} V_n + \sum_{n=1}^{\infty} b_n \epsilon^n \cos^n(\omega\tau + \beta_n) \\
\text{where } \omega &= \omega(\epsilon) = \sum_{k=0}^{\infty} \omega_k \epsilon^{2k}, \quad \beta_n = \beta_n(\epsilon) = \sum_{k=0}^{\infty} \beta_{n,k} \epsilon^{2k} \\
\eta(\tau|\epsilon) &= \eta_H + \eta_{osc} = \sum_{n=0}^{\infty} \epsilon^{2n} \eta_n + \sum_{n=1}^{\infty} c_n \epsilon^n \cos^n(\omega\tau + \gamma_n) \\
\text{where } \omega &= \omega(\epsilon) = \sum_{k=0}^{\infty} \omega_k \epsilon^{2k}, \quad \gamma_n = \gamma_n(\epsilon) = \sum_{k=0}^{\infty} \gamma_{n,k} \epsilon^{2k} \\
\theta(\tau|\epsilon) &= \theta_H + \theta_{osc} = \sum_{n=0}^{\infty} \epsilon^{2n} \theta_n + \sum_{n=1}^{\infty} d_n \epsilon^n \cos^n(\omega\tau + \delta_n) \\
\text{where } \omega &= \omega(\epsilon) = \sum_{k=0}^{\infty} \omega_k \epsilon^{2k}, \quad \delta_n = \delta_n(\epsilon) = \sum_{k=0}^{\infty} \delta_{n,k} \epsilon^{2k}.
\end{aligned}$$

To 3rd order in  $\epsilon$ , for example, the  $U(\tau)$  expansion becomes,

$$\begin{aligned}
U(\tau|\epsilon) &= U_0 + \epsilon^2 U_1 + (a_{1,0} + \epsilon^2 a_{1,1}) \epsilon \cos((\omega_0 + \epsilon^2 \omega_1)\tau + \alpha_{1,0} + \epsilon^2 \alpha_{1,1}) \\
&\quad + a_{2,0} \epsilon^2 \cos((\omega_0 + \epsilon^2 \omega_1)\tau + \alpha_{2,0})^2 + a_{3,0} \epsilon^3 \cos((\omega_0 + \epsilon^2 \omega_1)\tau + \alpha_{3,0})^3.
\end{aligned}$$

Solutions for the unknown constants, specifically the frequency  $\omega$ , amplitudes  $a$ ,  $b$ ,  $c$ ,  $d$ , and phase shift  $\alpha$ ,  $\beta$ ,  $\gamma$ ,  $\delta$ , are found through substitution of the form into the equations of motion (S1). The only free parameter is  $\epsilon$ . Thus, the form of the limit cycle can be accurately approximated close to the Hopf condition. Figures S3, S4, and S5 show typical examples of the approximation versus the numerics, where  $R = \sqrt{U^2 + V^2}$  is the nondimensional magnitude of the field. The base Hopf point in this calculation was  $x = 60$  (0.3 nm),  $S \approx 17.37$  (95  $\mu$ W), and the perturbation in parameter space was taken to be in  $S$  with fixed  $x$  ( $\nu_1 = 0$ ,  $\nu_2 = 1$ ). (Note: Here we have carried out the expansion to 5th order, and determined the period of oscillation to third order and the solution to 2nd order.)

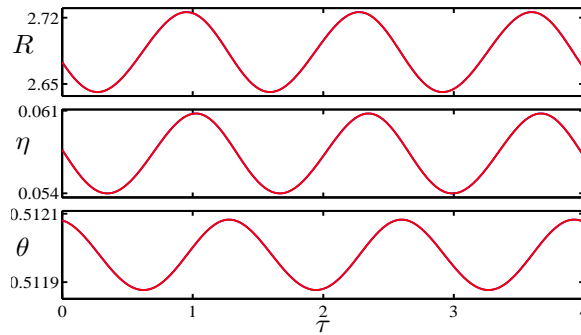


FIG. S3. Numerical solution (blue) and asymptotic expansion (red) of limit cycle near Hopf location. Here  $\epsilon^2 = 0.01$ ,  $S = S_{hopf} + \epsilon^2 \approx 17.38$  (95  $\mu$ W),  $x = 60$  (0.3 nm). Note that red curve obscures blue curve.

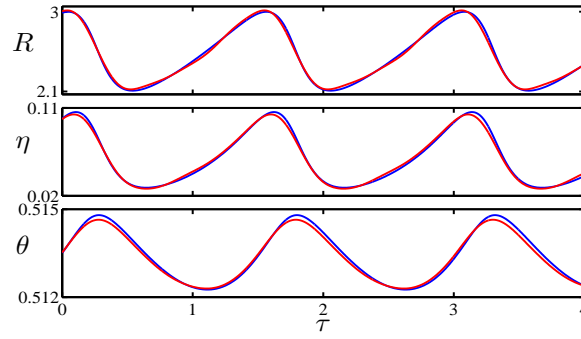


FIG. S4. Numerical solution (blue) and asymptotic expansion (red) of limit cycle near Hopf location. Here  $\epsilon^2 = 0.9$ ,  $S = S_{hopf} + \epsilon^2 \approx 18.27$  ( $105 \mu\text{W}$ ),  $x = 60$  ( $0.3 \text{ nm}$ ).

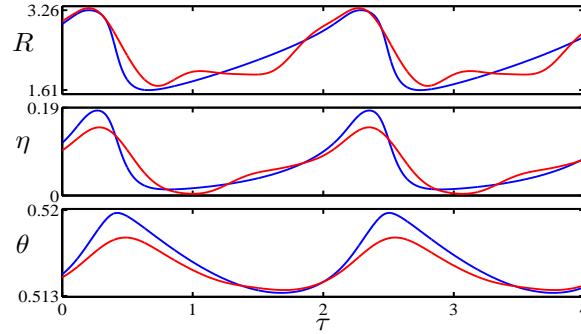


FIG. S5. Numerical solution (blue) and asymptotic expansion (red) of limit cycle near Hopf location. Here  $\epsilon^2 = 2$ ,  $S = S_{hopf} + \epsilon^2 \approx 19.37$  ( $118 \mu\text{W}$ ),  $x = 60$  ( $0.3 \text{ nm}$ ). Note that while the shape of the asymptotic limit cycle diverges from the numerics, the period remains relatively accurate.

Figure S6 compares the local approximation for the period of oscillation with the period from numerical integration.

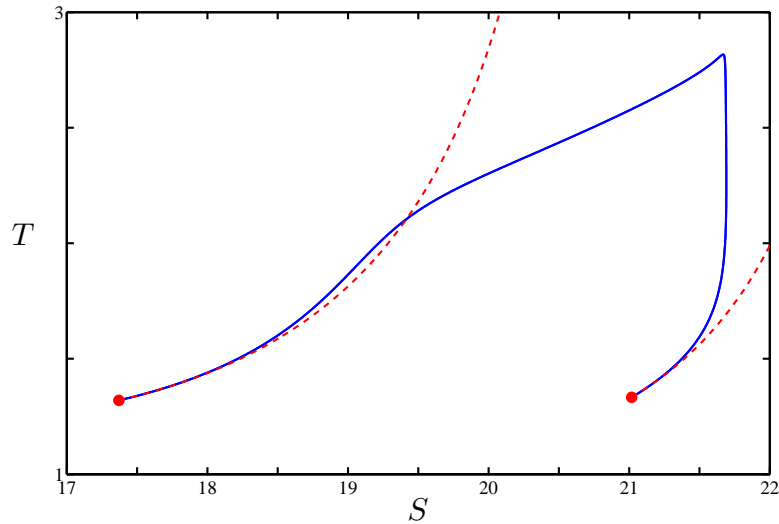


FIG. S6. Period of limit cycle  $T$  vs power  $S$ , from numerical solution (blue) and asymptotic expansions (red dashed). Two separate expansions from the Hopf locations (red circles) are shown: The limit cycle is born stable (supercritical) on the left, and unstable (subcritical) on the right. Here  $x = 60$  ( $0.3 \text{ nm}$ ).

The asymptotic expansion yields locally accurate approximations for the limit cycle's shape and period. This fit becomes less accurate as the nonlinearity of the oscillations increases.

A limitation of this approach is that it cannot predict the occurrence of the homoclinic bifurcation in parameter space. We found that the multiple time scale analysis yields more useful insight as the strength of the input signal is increased.

## S6. SURVEY OF PERIOD'S DEPENDENCY UPON PARAMETERS

Table S4 graphically depicts typical dependence of the full microdisk oscillation period on various physical parameters.

The time scale of the “spike” (red section in Fig. 2) increases linearly with  $V_{eff}$ , decays approximately with input power like  $P_{in}^{-1}$ , decays approximately with quality factor like  $Q^{-1}$ , and is unaffected by changes in detuning and  $\gamma_{Th}$ . These scalings are based upon analytic approximations of the 1D model, and are confirmed by numerical integration of the 2D model.

## S7. MULTIPLE TIME SCALE ANALYSIS

### Time Scale Separation

The separation of time scales can be formalized as the ratio of decay rates  $\gamma$  of the field ( $U, V$ ), free carriers ( $\eta$ ) and temperature ( $\theta$ ). Scaling system (S1) by the nondimensional parameter  $A_1^{-1}$ , and scaling time as  $\tau_1 = A_1\tau = \gamma_0 t$  gives,

$$\frac{dU}{d\tau_1} = -U - \frac{A_2 S^2}{A_1} U(U^2 + V^2) - \frac{A_3}{A_1} \eta U + \frac{A_4}{A_1} \eta V + \frac{A_5}{A_1} x V - \frac{A_6}{A_1} \theta V, \quad (\text{S5a})$$

$$\frac{dV}{d\tau_1} = -V - \frac{A_2 S^2}{A_1} V(U^2 + V^2) - \frac{A_3}{A_1} \eta V - \frac{A_4}{A_1} \eta U - \frac{A_5}{A_1} x U + \frac{A_6}{A_1} \theta U - \frac{A_7}{A_1}, \quad (\text{S5b})$$

$$\frac{d\eta}{d\tau_1} = -\frac{\gamma_{fc}}{\gamma_0} \left( \eta - \frac{A_9 S^4}{A_8} (U^2 + V^2)^2 \right), \quad (\text{S5c})$$

$$\frac{d\theta}{d\tau_1} = -\frac{\gamma_{Th}}{\gamma_0} \left( \theta - \frac{A_{11} S^2}{A_{10}} (U^2 + V^2) - \frac{A_{12} S^4}{A_{10}} (U^2 + V^2)^2 - \frac{A_{13} S^2}{A_{10}} \eta (U^2 + V^2) \right). \quad (\text{S5d})$$

If all the coefficients on the right hand side in one differential equation in the system are orders of magnitude larger than all coefficients of another differential equation in the system and all variables are of similar order, the first dynamic variable is said to evolve on a faster time scale. Equations (S5a) and (S5b) evolve on a faster time scale than the Eqs. (S5c) and (S5d) if the following conditions are met:

$$\frac{\gamma_{fc}}{\gamma_0} \ll 1, \quad (\text{S6})$$

$$\frac{\gamma_{Th}}{\gamma_0} \ll 1, \quad (\text{S7})$$

$$\frac{A_{3,4,5,6,7}}{A_1} \gtrsim 1 \quad (\text{S8})$$

$$\frac{A_2 S^2}{A_1} \gtrsim 1 \quad (\text{S9})$$

$$\frac{A_9 S^4}{A_8} \lesssim 1 \quad (\text{S10})$$

$$\frac{A_{11} S^2}{A_{10}}, \frac{A_{12} S^4}{A_{10}}, \frac{A_{13} S^2}{A_{10}} \lesssim 1. \quad (\text{S11})$$

For the devices considered in this work, conditions (S6), (S7), (S8), (S10), and (S11) are met, while condition (S9) is not (see Table S3). Nevertheless, we can treat Eqs. (S5a) and (S5b) as evolving on separate time scales from Eqs. (S5c) and (S5d) (we will address this in the next subsection).

We also observe that Eq. (S5c) evolves on a faster time scale than Eq. (S5d). Dividing Eqs. (S5c) and (S5d) by

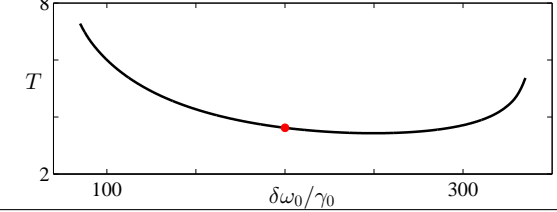
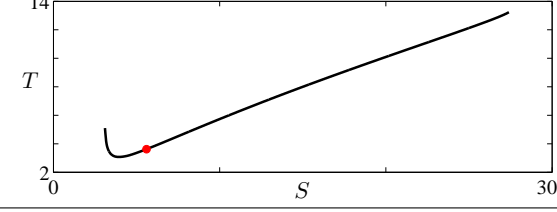
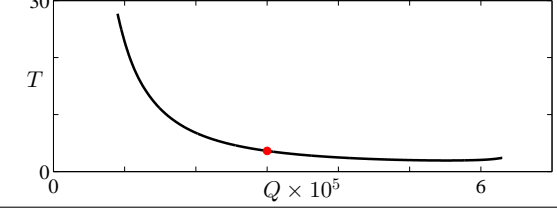
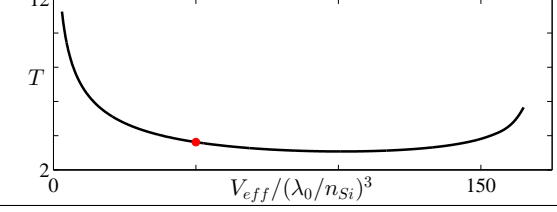
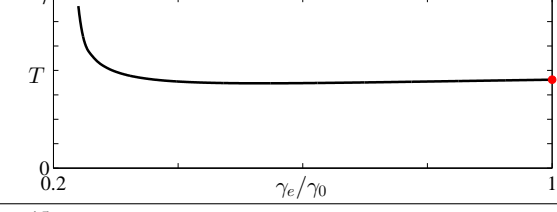
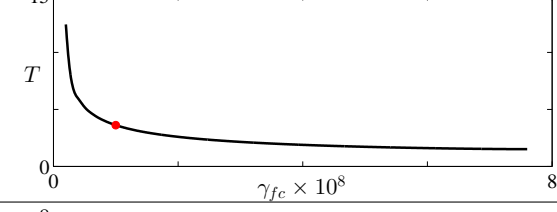
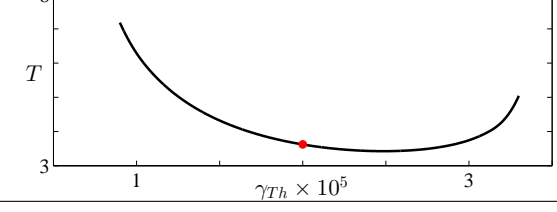
Parameter	General Behavior of Period	Figure
$\delta\omega_0/\gamma_0$	Non-monotonic	
$S$	Increasing	
$Q$	Decreasing	
$V_{eff}$	Non-monotonic	
$\gamma_e/\gamma_0$	Non-monotonic	
$\gamma_{fc}$	Decreasing	
$\gamma_{Th}$	Non-monotonic	

TABLE S4. Numerical survey of dependency of the nondimensional period of the limit cycle in parameter space. The red circle in each plot corresponds to values of the parameters given in Table S2, with  $\delta\omega_0/\gamma_0 = 200$  and  $P_{in} = 1$  mW ( $S = 56$ ).

$\gamma_{fc}/\gamma_0$ , and rescaling time as  $\tau_2 = (\gamma_{fc}/\gamma_0)\tau_1 = \gamma_{fc}t$  yields the following system:

$$\frac{dU}{d\tau_1} = -U - \frac{A_2 S^2}{A_1} U(U^2 + V^2) - \frac{A_3}{A_1} \eta U + \frac{A_4}{A_1} \eta V + \frac{A_5}{A_1} x V - \frac{A_6}{A_1} \theta V, \quad (\text{S12a})$$

$$\frac{dV}{d\tau_1} = -V - \frac{A_2 S^2}{A_1} V(U^2 + V^2) - \frac{A_3}{A_1} \eta V - \frac{A_4}{A_1} \eta U - \frac{A_5}{A_1} x U + \frac{A_6}{A_1} \theta U - \frac{A_7}{A_1}, \quad (\text{S12b})$$

$$\frac{d\eta}{d\tau_2} = -\eta + \frac{A_9 S^4}{A_8} (U^2 + V^2)^2, \quad (\text{S12c})$$

$$\frac{d\theta}{d\tau_2} = -\frac{\gamma_{Th}}{\gamma_{fc}} \left( \theta - \frac{A_{11} S^2}{A_{10}} (U^2 + V^2) - \frac{A_{12} S^4}{A_{10}} (U^2 + V^2)^2 - \frac{A_{13} S^2}{A_{10}} \eta (U^2 + V^2) \right). \quad (\text{S12d})$$

The time scales of Eqs. (S12c) and (S12d) can be formally separated if the following conditions are met:

$$\frac{\gamma_{Th}}{\gamma_{fc}} \ll 1, \quad (\text{S13})$$

$$\frac{A_8}{A_9 S^4} \lesssim 1 \quad (\text{S14})$$

$$\frac{A_{11} S^2}{A_{10}}, \frac{A_{12} S^4}{A_{10}}, \frac{A_{13} S^2}{A_{10}} \lesssim 1 \quad (\text{c.f. Eq. (S11)}) \quad (\text{S15})$$

For the devices considered in this work, conditions (S13), (S14), and (S15) are met. There is, of course, some error in this reduction, apparent in Fig. 4 of the main text: some change in  $\theta$  is visible when  $\eta$  is not on its nullcline,  $\frac{d\eta}{d\tau} = 0$ .

The full separation of time scales yields the system

$$\frac{dU}{d\tau_1} = -U - \frac{A_2 S^2}{A_1} U(U^2 + V^2) - \frac{A_3}{A_1} \eta U + \frac{A_4}{A_1} \eta V + \frac{A_5}{A_1} x V - \frac{A_6}{A_1} \theta V, \quad (\text{S16a})$$

$$\frac{dV}{d\tau_1} = -V - \frac{A_2 S^2}{A_1} V(U^2 + V^2) - \frac{A_3}{A_1} \eta V - \frac{A_4}{A_1} \eta U - \frac{A_5}{A_1} x U + \frac{A_6}{A_1} \theta U - \frac{A_7}{A_1}, \quad (\text{S16b})$$

$$\frac{d\eta}{d\tau_2} = -\eta + \frac{A_9 S^4}{A_8} (U^2 + V^2)^2, \quad (\text{S16c})$$

$$\frac{d\theta}{d\tau_3} = -\theta + \frac{A_{11} S^2}{A_{10}} (U^2 + V^2) + \frac{A_{12} S^4}{A_{10}} (U^2 + V^2)^2 + \frac{A_{13} S^2}{A_{10}} \eta (U^2 + V^2), \quad (\text{S16d})$$

where  $\tau_1 = \gamma_0 t$ ,  $\tau_2 = \gamma_{fc} t$ , and  $\tau_3 = \gamma_{Th} t$ , with  $\tau_1 \gg \tau_2 \gg \tau_3$ .

### Limitations of Multiple Times Scales

*Condition S9*—Numerically, removing the  $A_2 S^2$  term in Eqs. (S1a) and (S1b) has negligible effect on the system's fixed points and dynamic behavior (the accuracy of the 2D reduction in representing the 4D model is further confirmation of this assertion). Thus, we will remove the terms in Eqs. (S1a) and (S1b) with coefficient  $A_2 S^2$  in our multiple time scale analysis. This is reasonable, given that the magnitude of the  $A_2 S^2$  is much smaller than other terms in Eqs. (S1a) and (S1b). (We have quantified the error introduced by removing this term and found that it is  $\mathcal{O}(\frac{A_2 S^2}{A_1})$ .) At a power higher than  $S = 150$ , ( $P_{in} = 7$  mW), the term  $A_2 S^2$  is within an order of magnitude of  $A_1$ , and thus we would expect this nonlinearity to become more important. In addition, due to its nonlinearity, we expect this term to affect the spike during the limit cycle, and our model excluding this term to be least accurate at the spiking event.

In the regime of low power (low  $S$ ) condition (S14) breaks down. Using the standard parameter values given in Table S3, we find  $S \gtrsim 95$ , or that this condition is satisfied when  $P_{in} > 3$  mW. This lower bound for  $P_{in}$  is actually more strict than necessary for a satisfactory separation of times scales: comparing the magnitude of  $A_9 S^4$  to the largest term in Eq. (S1d) gives a more generous condition. Assuming an order of magnitude difference between the terms suggests the time scale separation begins to break down at  $S \approx 35$ , or powers lower than approximately  $380 \mu\text{W}$ .

In the regime of high power, (high  $S$ ), conditions (S10) and (S11) breaks down. The strictest of these four relations for our parameter values is (S10). The term  $A_9 S^4$  is an order of magnitude greater than  $A_8$  when  $S > 170$ , ( $P_{in} = 9\text{mW}$ ).

### 1D Model

After reducing the 4D system to a 2D system, as described in the main text, we can further reduce to a 1D model, as presented in Eqs. (4) and (5):

$$\theta = \frac{A_5 x + A_4 \eta}{A_6} \pm \frac{\sqrt{-A_3^2 \eta^4 - 2A_1 A_3 \eta^3 - A_1^2 \eta^2 + \sqrt{\frac{A_7^4 A_9 S^4}{A_8}} \eta^{3/2}}}{A_6 \eta}, \quad (\text{S17})$$

$$\begin{aligned} \dot{\theta} = & -\frac{A_{10} A_5 x}{A_6} + \frac{\sqrt{A_8} A_{11}}{\sqrt{A_9}} \sqrt{\eta} + \left( \frac{A_8 A_{12}}{A_9} - \frac{A_{10} A_4}{A_6} \right) \eta \\ & + \frac{\sqrt{A_8} A_{13}}{\sqrt{A_9}} \eta^{3/2} \pm \frac{A_{10} \sqrt{-A_3^2 \eta^4 - 2A_1 A_3 \eta^3 - A_1^2 \eta^2 + \sqrt{\frac{A_7^4 A_9 S^4}{A_8}} \eta^{3/2}}}{A_6 \eta}. \end{aligned} \quad (\text{S18})$$

This is a parameterized 1D system with two branches (represented by the  $\pm$ ) that approximate the two slow sections of the limit cycle. The boundaries of the one dimensional limit cycle are the transition points between these two solution branches, which are defined by the condition

$$\frac{d\theta}{d\eta} = 0. \quad (\text{S19})$$

Converting the condition to a polynomial expresses the critical  $\eta$  values as roots to a tenth order polynomial. Note from Eq. (S17) that the expression is independent of  $x$ . This allows us to numerically solve the expression while retaining dependence upon the control parameter  $x$ . This ‘‘critical  $\eta$ ’’ condition has two real, positive solutions,  $\eta_1^*$  and  $\eta_3^*$ . We can also find the ‘‘collection’’ points on each of the two branches that the solution jumps to,  $\eta_2^*$  and  $\eta_4^*$ . Plugging the solutions for  $\eta$  into (S17) gives the maximum and minimum  $\theta$  values of the limit cycle, and into Eq. (S18) the corresponding  $\dot{\theta}$  values. The  $\eta$  solutions have no dependence upon detuning  $x$ , while  $\theta$  and  $\dot{\theta}$  have linear dependence upon detuning:

$$\theta_{max}^* = \theta_1^* = \frac{A_5 x}{A_6} + g_1(S), \quad (\text{S20a})$$

$$\theta_{min}^* = \theta_3^* = \frac{A_5 x}{A_6} + g_2(S), \quad (\text{S20b})$$

$$\dot{\theta}_i^* = \frac{-A_{10} A_5 x}{A_6} + h_i(S), \quad (\text{S20c})$$

where  $g_1$ ,  $g_2$ , and  $h_i$  are implicit functions of  $S$  defined as roots of a polynomial. Figure 4 in the main text labels these points for the 1D limit cycle.

Figure S7 shows the dependency of the shape of the 1D limit cycle upon the control parameters. Shifts in detuning translate the limit cycle without changing its shape. Changes in driving power both translate and adjust the shape of the limit cycle.

### Analytic Approximation to 1D Model

The functions  $g_{1,2}$  and  $h_i$  from Eq. (S20) implicitly depend upon all the problem parameters  $A_1$  through  $A_{13}$ . We can approximate that dependence using Taylor series near the critical  $\eta$  condition. According to our nondimensionalization, we expect that  $\eta_1^*$  will be  $\mathcal{O}(1)$ , while the  $\eta_3^*$  will be very small. Under these assumptions, we find

$$\begin{aligned} \eta_1^* & \approx \frac{A_3 - 3A_1}{A_1 + 5A_3} + \frac{4A_7 A_9^{1/4} S}{A_8^{1/4} (A_1 + 5A_3)}, \\ \eta_3^* & \approx \left( \frac{A_7 A_9^{1/4} S}{4A_8^{1/4} A_4} \right)^{4/5}. \end{aligned}$$

Using these two values we can find expressions for all four locations on the limit cycle in terms of any desired parameter. For example, the onset of oscillations (Hopf bifurcation) occurs when  $\dot{\theta}_3^* = 0$  for increasing detuning.

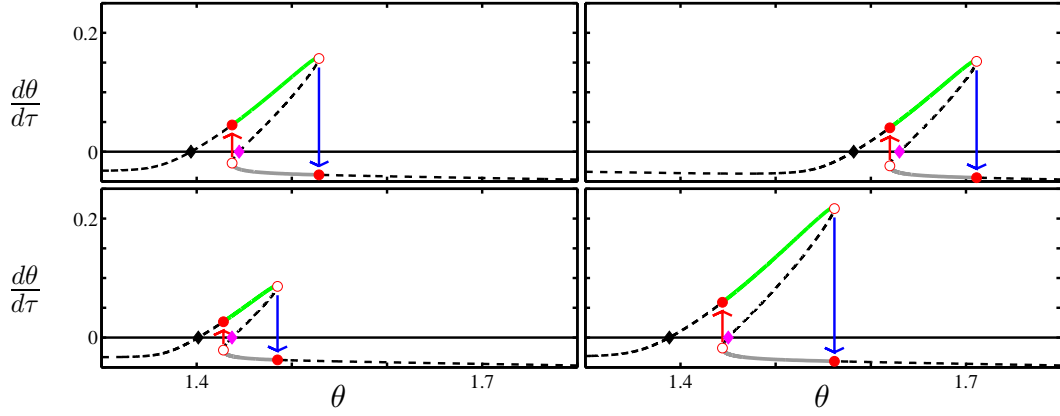


FIG. S7. Change of 1D limit cycle with respect to detuning and power. Shown are nullclines of  $\eta$  (dashed), unstable fixed points (filled diamonds), and points of interest in the 1D reduction (filled and open circles). Arrows indicate instantaneous jumps (from time scale separation). Parameter values:  $(S = 56, x = 168)$ ,  $(S = 56, x = 190)$ ,  $(S = 42, x = 168)$ ,  $(S = 67, x = 168)$ . Changes in detuning shift the limit cycle while changes in power elongate or collapse limit cycle branches.

Plugging the approximate expression for  $\eta_3^*$  into Eq. (S18) yields a general expression of the Hopf condition for all control parameters in the problem. Similarly, the onset of oscillations (Hopf bifurcation) for decreasing detuning occurs when  $\theta_1^* = 0$ . These approximations for the Hopf location are compared with the actual Hopf location from the 4D system and the 1D system in Fig. S8.

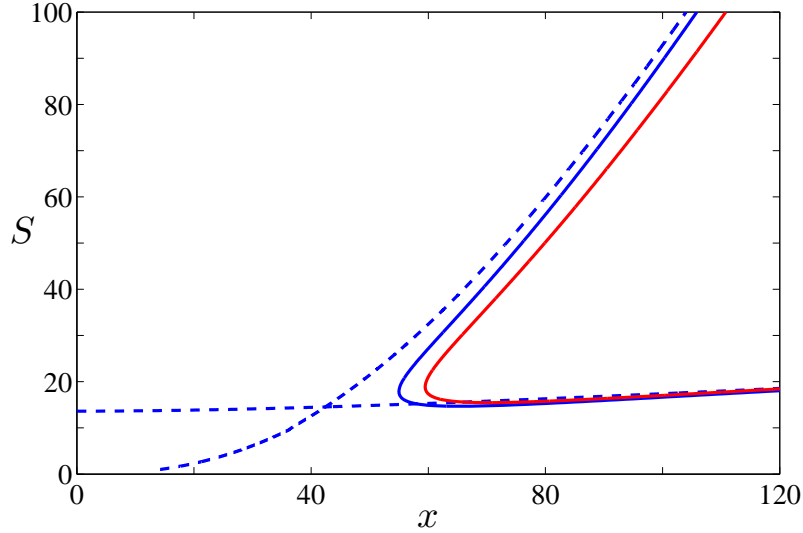


FIG. S8. Onset of oscillations with respect to detuning from resonance. The Hopf bifurcation of the four dimensional system (red) is compared with the onset of oscillations for the 1D system (blue) and the analytic approximation for the 1D system (dashed blue). Power ranges from 0 mW to 3.16 mW, Detuning ranges from 0 nm to 0.5 nm. Note that the homoclinic bifurcation is not shown.

\* dmabrams@northwestern.edu

† AlexanderSlawik2015@u.northwestern.edu

‡ kartik.srinivasan@nist.gov

[1] T. J. Johnson, M. Borselli, and O. Painter, Optics Express **14**, 817 (2006).